

# Interpreting the H<sub>I</sub> 21 cm cosmology maps through Largest Cluster Statistics. Part II. Impact of the realistic foreground and instrumental noise on synthetic SKA1-Low observations

**Samit Kumar Pal,<sup>a,1</sup> Saswata Dasgupta,<sup>b,c,a</sup> Abhirup Datta,<sup>a</sup> Suman Majumdar,<sup>a,d</sup> Satadru Bag,<sup>e,f</sup> and Prakash Sarkar<sup>g</sup>**

<sup>a</sup>Department of Astronomy, Astrophysics & Space Engineering, Indian Institute of Technology Indore, Indore 453552, India

<sup>b</sup>Institute of Astronomy, University of Cambridge, Cambridge, UK.

<sup>c</sup>Kavli Institute for Cosmology, University of Cambridge, Cambridge, UK.

<sup>d</sup>Department of Physics, Blackett Laboratory, Imperial College, London SW7 2AZ, U. K.

<sup>e</sup>Technical University of Munich, TUM School of Natural Sciences, Physics Department, James-Franck-Straße 1, 85748 Garching, Germany

<sup>f</sup>Max-Planck-Institut für Astrophysik, Karl-Schwarzschild Straße 1, 85748 Garching, Germany

<sup>g</sup>Department of Physics, Kashi Sahu College, Seraikella, Jharkhand - 833219, India

---

<sup>1</sup>Corresponding author.

E-mail: [palsamitkumar@gmail.com](mailto:palsamitkumar@gmail.com)

**Abstract.** The Largest Cluster Statistics (LCS) analysis of the redshifted 21 cm maps has been demonstrated to be an efficient and robust method for following the time evolution of the largest ionized regions (LIRs) during the Epoch of Reionization (EoR). The LCS can, in principle, constrain the reionization model and history by quantifying the morphology of neutral hydrogen (H<sub>I</sub>) distribution during the different stages of the EoR. Specifically, the percolation transition of ionized regions, quantified and constrained via LCS, provides a crucial insight about the underlying reionization model. The previous LCS analysis of EoR 21 cm maps demonstrates that the convolution of the synthesized beam of the radio interferometric arrays, e.g. SKA1-Low with the target signal, shifts the apparent percolation transition of ionized regions towards the lower redshifts. In this study, we present an optimal thresholding strategy to reduce this bias in the recovered percolation transition. We assess the robustness of LCS analysis of the 21 cm maps in the presence of antenna-based gain calibration errors and instrumental noise for SKA1-Low. This analysis is performed using synthetic observations simulated by the 21cmE2E pipeline, considering SKA1-Low AA4 configuration within a radius of 2 km from the array centre. Our findings suggest that a minimum of 1500 hours of observation ( $\text{SNR} \gtrsim 3$ ) are required for the LCS analysis to credibly suppress the confusion introduced by thermal noise. Further, we also demonstrate that for a maximum antenna-based calibration error tolerance of  $\sim 0.05\%$  (post calibration), the reionization history can be recovered in a robust and relatively unbiased manner using the LCS.

**Keywords:** reionization, non-gaussianity, cosmological simulations, Statistical sampling techniques

---

## Contents

<b>1</b>	<b>Introduction</b>	<b>1</b>
<b>2</b>	<b>Simulations of the radio sky</b>	<b>3</b>
2.1	Seminumerical simulation of reionization	3
2.2	Astrophysical foregrounds	3
2.2.1	Diffuse emission	4
2.2.2	Extragalactic point sources	4
<b>3</b>	<b>Simulations of observations</b>	<b>5</b>
3.1	Telescope model	6
3.2	Gain calibration error	6
3.3	Instrumental noise	8
<b>4</b>	<b>Percolation Transition &amp; LCS</b>	<b>10</b>
4.1	Binarization of the image cubes	11
<b>5</b>	<b>Results</b>	<b>12</b>
5.1	Effect of thresholding	12
5.2	Effect of gain calibration error	14
5.3	Effect of instrumental noise	17
<b>6</b>	<b>Summary and discussion</b>	<b>19</b>
<b>7</b>	<b>Acknowledgements</b>	<b>21</b>

---

## 1 Introduction

The Cosmic Dawn (CD) and Epoch of Reionization (EoR) mark a significant period in the cosmic timeline, yet it remains one of the least understood epochs in the evolution of the universe. During this epoch, the UV and X-ray photons started to ionize the neutral hydrogen in the intergalactic medium (IGM). Studies of the absorption spectra of Ly $\alpha$  from high-redshift quasars suggest that reionization was nearly complete by  $z \sim 6$  [1]. Our present knowledge suggests that the process of reionization began when the first stars and galaxies formed in the over-density regions. This process led to the ionization of nearby gas and the formation of individual ionized bubbles. However, the exact details of the reionization process, such as the nature and properties of the ionizing sources and the morphology and topology of the ionized bubbles at different stages of reionization, still remain uncertain.

The redshifted H $\text{I}$  21 cm signal arises from the spin-flip transition of electrons in the ground state. The observation of the redshifted H $\text{I}$  21 cm signal serves as a direct window into the state of hydrogen in the IGM and, thereby, can potentially be used to study this complex period. By measuring spatial fluctuations in the 21 cm signal with radio interferometry, it

is possible to create tomographic maps of H<sub>I</sub> regions throughout the sky. The detection of the redshifted H<sub>I</sub> 21 cm signal from CD/EoR is a pivotal science goal of first-generation radio interferometers such as GMRT [2], MWA [3], LOFAR [4], and HERA [5]. Due to the low signal-to-noise (SNR) ratio, these interferometers were focused on statistical detection of the target signal, such as the power spectrum. Next-generation radio interferometers such as HERA and SKA-Low are expected to precisely measure the H<sub>I</sub> 21 cm signal power spectrum (PS) from CD/EoR with high precision. However, the detection of 21 cm signal is very challenging because of the bright astrophysical foreground, which is 4 – 5 orders of magnitude brighter than the target signal [6–12]. In addition, along with foreground, calibration errors [13–16], ionospheric disturbances [17–19], and instrumental effects [20] introduce distortion in the target signal.

Although the PS is a powerful tool, the EoR 21 cm signal is expected to be strongly non-Gaussian, and the PS alone could not fully describe it. Therefore, higher-order statistics, such as the bispectrum [21, 22] and trispectrum [23] are necessary to capture this non-Gaussian nature. The image-based e.g. statistics Minkowski functionals (MFs) [24–33] and Minkowski Tensors also provide a useful way to explore this morphological and topological evolution of reionization. Additionally, Percolation theory [29, 30, 34–36], granulometry [37], persistence theory [38], and Betti numbers [39, 40] are some of the methods employed to analyze the topological phases of ionized hydrogen (H<sub>II</sub>) regions during the EoR.

It is generally accepted that conclusions from these image-based methods depend on detecting a large number of H<sub>II</sub> regions across different stages and sizes. However, the study by Bag et al. [29, 30] demonstrates that identifying only the largest ionized region (LIR) is sufficient to infer the percolation process. To reach this conclusion, they introduced a novel statistic named Largest Cluster Statistics (LCS), along with a shape-finding algorithm. The LCS analysis of the redshifted 21 cm maps has been demonstrated to be an efficient and robust method for tracking the time evolution of the LIRs during the EoR. The LCS can constrain the reionization model and history by quantifying the morphology of neutral hydrogen distribution during the different stages of the EoR. Specifically, the percolation transition of ionized regions, quantified and constrained via LCS, provides a crucial insight about the underlying reionization model [32]. Our previous work, Dasgupta et al. [33], demonstrates how the convolution of the synthesized beam of the radio interferometric arrays, e.g. SKA1-Low with the target signal, can affect our conclusion about the percolation of H<sub>II</sub> regions during reionization. They showed that the apparent percolation transition of ionized regions shifted towards the later stage of reionization, depending upon the array synthesized beam of SKA1-Low and thresholding formalism used in noisy data.

Motivated by this, we present an optimal thresholding strategy to reduce this bias in the recovered percolation transition in this study. Furthermore, we assess the robustness of our LCS analysis of the 21 cm maps under various kinds of foreground corruption conditions. For this purpose, we consider two sources of foreground contamination: a) extra-galactic point sources and b) diffuse synchrotron and free-free emission. For all of these sky models, we consider the antenna-based gain calibration errors to estimate the maximum tolerance level to recover the reionization history in a robust and relatively unbiased manner using LCS. In

addition, we have also investigated the impact of instrumental noise for SKA1-Low on this analysis via the synthetic observations simulated by the 21cmE2E pipeline <sup>1</sup>. This analysis is done by diagnostic tool SURFGEN2 [29, 30] to estimate the LCS and gain insights into the percolation of HII regions during the EoR.

This paper is organized as follows: In Section 2, we discuss the simulation of the radio sky. Section 3 describes our end-to-end simulation and the methodology used to incorporate antenna-based gain calibration errors and instrumental noise on synthetic SKA1-Low observations. The analysis formalism is presented in Section 4, followed by the results in Section 5. Finally, we summarize and discuss our findings in Section 6. We used best-fitted cosmological parameters from the WMAP five-year data release that have been used throughout the paper, which details as follows:  $h = 0.7$ ,  $\Omega_m = 0.27$ ,  $\Omega_\Lambda = 0.73$ ,  $\Omega_b h^2 = 0.0226$  [41].

## 2 Simulations of the radio sky

We investigate the robustness of LCS analysis to study the evolution of the largest ionized region during different stages of reionization. This analysis uses synthetic SKA1-Low observations generated from a realistic simulation based on 21cmE2E-pipeline. This section describes the simulation of sky models. The sky models consist of the H I signal and astrophysical foreground within redshift range  $7.2 < z < 8.8$ , corresponding to frequency  $\sim 144 - 173$  MHz.

### 2.1 Seminumerical simulation of reionization

In this section, we provide a brief review of the simulation of the H I fields at different stages of the EoR. For detailed information, readers can refer to Section 2 of Dasgupta et al. [33]. To construct the brightness temperature maps of H I 21 cm signal, we used the REIONYUGA simulation [42–44]. This simulation employs a semi-numerical approach based on excursion set formalism. The REIONYUGA utilizes an N-body simulation to create the distribution of dark matter at a given redshift. Next, a Friends-of-Friends (FoF) halo finding algorithm was used to detect the occurrence of the collapse of dark-matter halos inside this distribution of matter. The first light sources, which emit reionizing photons, are formed halos. The ionization fields created via excursion set formalism are thereafter transformed into the field of 21 cm brightness temperature. For our analysis, we used the existing simulated H I 21 cm maps from Dasgupta et al. [33]. These maps are coeval boxes, where each box measures  $143.36$  cMpc on each side and is distributed over a mesh consisting of a  $256^3$  grid volume. A detailed study of the evolution of the LCS along a lightcone to understand how the lightcone effect biases the percolation curve and affects the distinguishability of source models is presented in Potluri et al. (in prep.).

### 2.2 Astrophysical foregrounds

One of the major contaminants of CD/EoR experiments is the astrophysical foreground. Their brightness is 4 – 5 orders of magnitude higher than the faint 21 cm signal. The primary

---

<sup>1</sup><https://gitlab.com/samit-pal/21cme2e>

components in the foreground include diffuse galactic synchrotron radiation, galactic and extra-galactic free-free radiation and extra-galactic point sources. The foreground emission is expected to be spectrally smooth. However, calibration and instrumental effects introduce additional unsmooth structures. We considered two sources of foreground contamination: diffuse emission and extra-galactic point sources. The foreground contributions are detailed below.

### 2.2.1 Diffuse emission

The diffuse galactic emissions are dominated by the synchrotron and free-free emissions. Being large-scale structures, these are sensitive to shorter baselines. The diffuse synchrotron and free-free emission foregrounds were simulated using models outlined in [45, 46]. The Planck Sky Model (PSM) at 217 GHz are used to simulate the diffuse maps. At each pixel  $p$ , the brightness of these emissions is quantified using brightness temperature  $T_s$ . These are modelled as power laws:

$$T(\nu, p) = T_s \left( \frac{\nu}{\nu_0} \right)^{\beta_s(\nu, p)} \quad (2.1)$$

where  $\beta_s$  is the spectral index. The all-sky amplitudes for synchrotron and free-free emissions simulations are publically available on the Planck Legacy Archive<sup>2</sup>. Using the HEALPIX routines, we degrade and smooth these maps to our desired NSIDE<sup>3</sup> and resolution. The amplitude of diffuse emission is determined from the PSM at 217 GHz with a resolution of NSIDE=2048. To determine the spectral index map of synchrotron emission, we used 217 GHz and 353 GHz synchrotron maps at NSIDE=2048. Therefore, the spectral index varies in each pixel for synchrotron maps, whereas free-free emission  $\beta_{\text{ff}} = -2.13$  [46], is constant in all the pixels. These spectral indices and brightness temperature maps obtained at 217 GHz are used to extrapolate to the frequencies of interest using the equation 2.1. Here, we simulated the diffused foregrounds at  $\alpha = 0$  h and  $\delta = -30^\circ$  field and rotated the centre of the field to our pointing centre.

We generate image cubes by including the calibration error to explore the robustness of our LCS analysis. A more detailed discussion is provided in Section 3.2. In a synthetic SKA1-Low observation, the residual contamination left in the image cube will impact the evolution history of reionization. Following Mazumder et al. [16], we vary the foreground residual amplitude from  $10^{-3}\%$  to  $10^{-2}\%$  of the actual sky emission of our simulation. This variation is used to study its impact on the estimated LCS evolution.

### 2.2.2 Extragalactic point sources

In addition to the galactic and extra-galactic diffuse emission, the total foreground emission is also affected by extra-galactic point sources. These extra-galactic point sources are often compact and finite in size. This study uses the Tiered Radio Extra-galactic Continuum Simulation (T-RECS)[47] catalogue. At a frequency of 150 MHz, the flux values of the sources range from 3.1 mJy to 0.6 Jy. The fluxes were transformed to extrapolate to the

<sup>2</sup><https://pla.esac.esa.int/#maps>

<sup>3</sup>The resolution of the map is defined by the NSIDE parameter

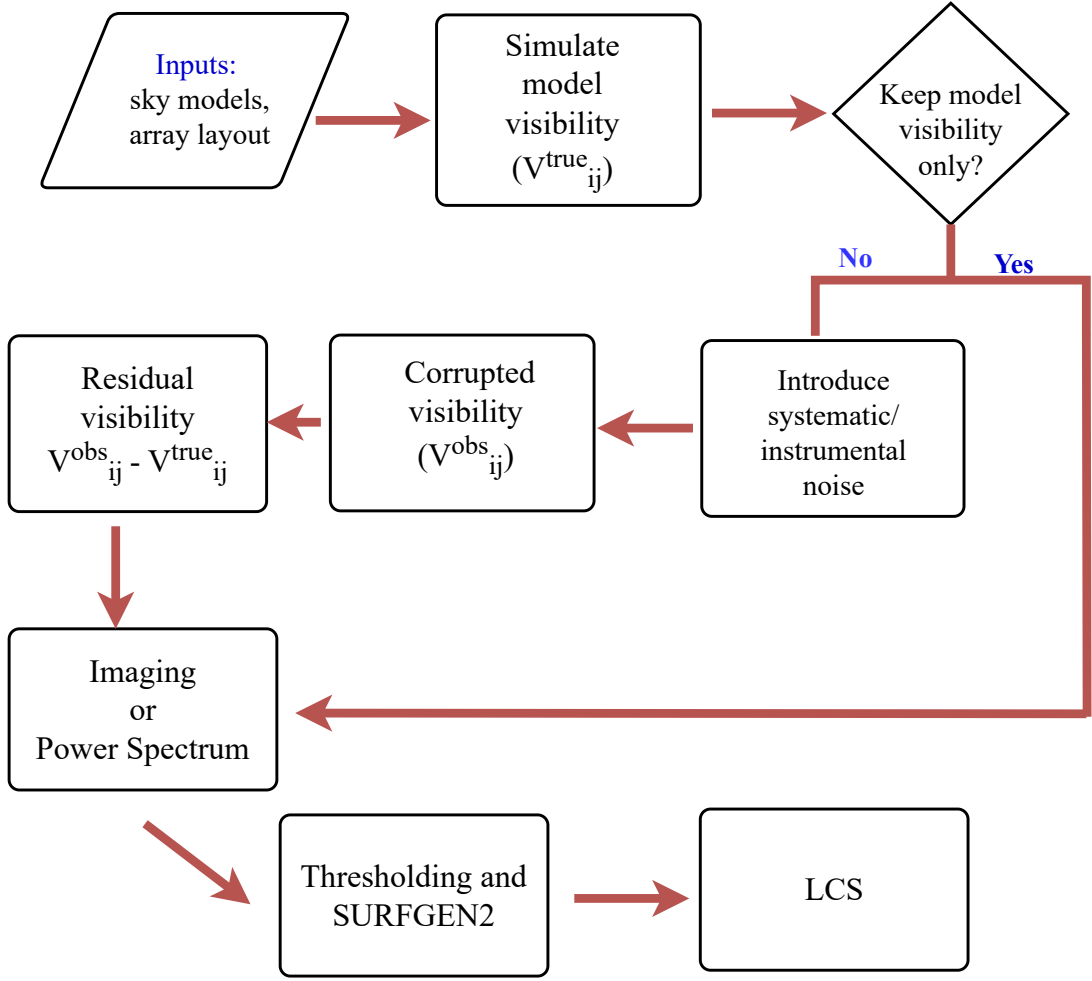


**Figure 1:** Schematic diagram of the 21cmE2E-pipeline based on OSKAR and CASA software. This pipeline is used to estimate LCS from 21 cm observation results.

frequencies of interest using the relationship  $S_\nu \propto \nu^{-\alpha}$ , where  $\alpha$  is  $-0.8$ . These extra-galactic point sources mainly comprises of star-forming galaxies and radio-quiet quasars. For a detailed description of the T-RECS catalogue model, readers can refer to [16, 47]. The T-RECS catalogue covers the  $(4^\circ)^2$  sky area. However, we generated image cubes only for the central region, covering  $(\sim 1.5^\circ)^2$  fields. This was done to match the field of view (FoV) of the input of the input H<sub>I</sub> maps from REIONYUGA, depending on the redshift of observation. Bright sources in the beam sidelobes present challenges for data calibration in real observations. However, these effects were not considered in this work.

### 3 Simulations of observations

This section outlines the synthetic observation with SKA1-Low to simulate the radio sky discussed in Section 2. Figure 1 shows the schematic diagram of the 21cmE2E pipeline. This

pipeline is based on the OSKAR<sup>4</sup> and CASA<sup>5</sup> [48]. The OSKAR [49] package generates the simulated visibility based on the input sky model, observational parameters, and telescope specifications. CASA is then used to create image cubes from the simulated visibilities. We simulated only 30 minutes of observation, which will be restricted to  $\pm 0.15$  minutes around the transit time of the target EoR field for this study to reduce computational costs. The field of view centred at  $\alpha = 15$  h and  $\delta = -30^\circ$ . The integration time for the simulation was set to 120 seconds. In the simulated H<sub>I</sub> 21 cm cube, one axis represents the line-of-sight (LoS) or frequency axis. The cubes were then divided into slices based on their frequency resolution. Each slice was assigned a frequency label corresponding to the comoving distance from the observer. The slices of the 21 cm maps were converted from comoving Mpc (cMpc) to angular coordinates on the sky plane. These angular maps were then processed through the 21cmE2E pipeline. Images were produced using the briggs weighting scheme with robust parameter 0.5 using CASA `tclean` task. The frequency-labeled slices were stacked, and final image cubes were made for further analysis. It is noted that the observed H<sub>I</sub> maps have the same size as the input H<sub>I</sub> maps. The pixel size was chosen to match the size of the input H<sub>I</sub> maps.

### 3.1 Telescope model

The SKA1-Low is one of the most sensitive upcoming radio interferometers. It is expected to make tomographic maps of the H<sub>I</sub> 21 cm signal from the EoR [50]. The construction of the SKA1-Low radio interferometer is progressing rapidly in Inyarrimanha Ilgari Bundara, Western Australia. The telescope will consist of 512 stations with a maximum baseline of approximately 74 km. Since the EoR signal is mostly present on shorter baselines, it corresponds to large angular scales. We used the array assembly 4 (AA4) configuration of SKA1-Low within a radius of 2 km from the array centre and excludes the longer baselines [51]. This compact array configuration consists of 296 stations. The station layout of SKA1-Low is shown in Figure 2.

### 3.2 Gain calibration error

The main observable quantity of the radio interferometers is the visibility. However, non-ideal radio interferometers do not directly measure the true visibility,  $V_{ij}^{\text{true}}$ , for each baseline formed by the  $i$ th and  $j$ th antennas. Instead, they measure the observed visibility,  $V_{ij}^{\text{obs}}$ . The relationship between the observed and true visibility (assuming implicit time and frequency dependence) is given by

$$V_{ij}^{\text{obs}} = g_i g_j^* V_{ij}^{\text{true}} + n_{ij} \quad (3.1)$$

Where  $g_i$  &  $g_j^*$  is the complex antenna gain term and  $n_{ij}$  is the noise on  $ij$ th baseline. However, the true visibility,  $V_{ij}^{\text{true}}$ , can be measured by a perfectly calibrated noiseless interferometer. To obtain the true visibility, we need to calibrate the observation. During calibration, we solve the gain factors  $g_i$  &  $g_j$  to minimize the chi-square between true and observed visibility. However, the accuracy of calibration is limited by the SNR. In an ideal scenario, the gain

<sup>4</sup><https://ska-telescope.gitlab.io/sim/oskar/>

<sup>5</sup><https://casa.nrao.edu/>



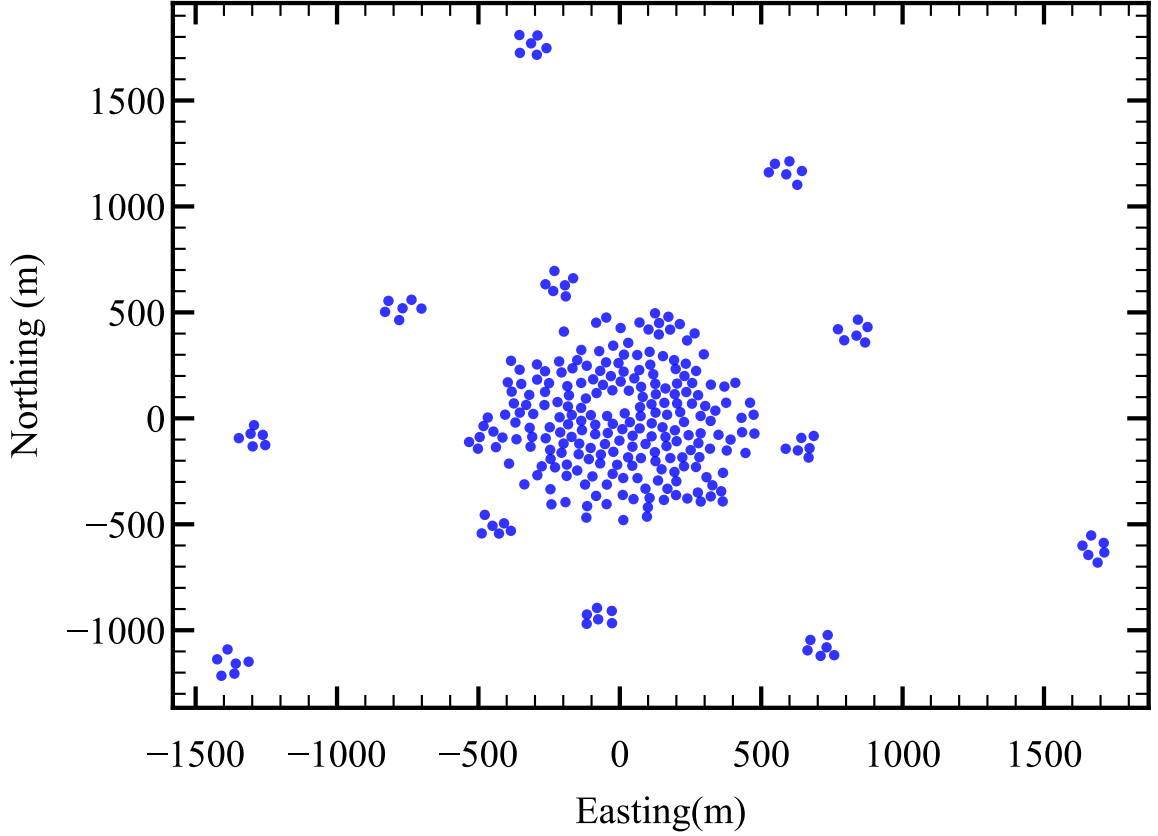


**Figure 2:** Telescope layout of the SKA1-Low array assembly 4 (AA4) configuration within a radius of 2 km from the array centre.

factor should be unity. However, an analytical solution of Equation 3.1 for the desired parameter is intractable. Given  $N$  antennas, there are  $N(N-1)/2$  baselines. These baselines correspond to  $N(N-1)/2$  true visibilities, which we want to solve along with  $N$  antenna gain factors. This process of correcting the antenna gain is known as self-calibration or direction-independent calibration. In 21 cm experiments, either sky-based or redundant calibration techniques are used. The accurate calibration is essential because the uncalibrated part of gains or residual gains will propagate into the subsequent steps, thereby introducing errors during the extraction of the target signal. The residual complex gain from the antenna ‘i’ can be modelled by

$$\delta g_i = (1 + \delta a_i) e^{-\delta \phi_i} \quad (3.2)$$

where  $\delta a_i$  &  $\delta \phi_i$  are the errors in amplitude and phase. The  $\delta a_i$  is dimensionless and  $\delta \phi_i$  is measured in degree. The efficiency of the calibration is characterized by minimizing of  $\delta a_i$  and  $\delta \phi_i$ . Due to the faint nature of 21 cm signal, achieving an  $\text{SNR} \geq 1$  becomes a daunting challenge. This work quantifies the degree of accuracy needed for the LCS analysis for future SKA1-Low observations to study the percolation process during reionization.

In order to add the calibration error in this simulation, we assumed that the errors in amplitude and phase follow a zero-mean Gaussian distribution with a specified standard deviation (see

equation 3.2). The calibration errors are sampled randomly with different standard deviations at the level of  $10^{-3}\%$  to  $10^{-2}\%$  in amplitude and  $10^{-3}$  to  $10^{-2}$  degree in phase. These errors are applied to each time domain of a single observation. We assumed that the calibration errors were uncorrelated for multiple observations. Therefore, calibration errors can be suppressed by averaging the deep observations. We focus on the deep observations with a total duration of 1000 h. In this work, we simulated the input sky with 30 min of continuous track observation. Therefore, to achieve the 1000 h of integration time, the same patch of sky must be observed repeatedly 2000 times. After the final post-calibration and averaging, the standard deviations are calculated for each time domain of a single observation. The calibration error is multiplied by the model visibility data. This creates the residual visibility after subtracting the foreground models using CASA `uvsub` task. This `uvsubed` residual visibilities dataset is used to make image cubes for LCS analysis. The top panel of Figure 3 shows the slices of the observed brightness temperature of  $\bar{x}_{\text{HI}} \approx 0.55 (z = 7.76)$ . The top-left panel shows the observed H<sub>I</sub> map without any bias due to corruption. The middle and right top panel shows the residual maps after introducing calibration errors of  $\sim 0.05\%$  &  $\sim 0.09\%$ , respectively. The bottom panel shows the recovered H<sub>II</sub> regions identified using the triangle algorithm. In these maps, the white (black) regions represent the ionized (neutral) regions. The higher calibration errors reduce the dynamic range of the image. Residual foregrounds pose a significant challenge in making the map of ionized regions. At the calibration inaccuracy of  $\sim 0.09\%$ , the triangle method failed to retrieve the regions from the residual field.

### 3.3 Instrumental noise

In this Section, we discuss how the sensitivity of the system, in conjunction with total integration time, affects the synthesized map. We added an uncorrelated Gaussian noise to the simulated visibilities. This is achieved by adding randomly generated values selected from a zero-mean Gaussian distribution to the complex visibility amplitudes for each frequency channel, time integration, baseline, and polarization. The amplitude of the thermal noise per baselines following the radiometer equation [52] is given by

$$\sigma_N = \frac{2k_B T_{\text{sys}}}{A_{\text{eff}} \sqrt{\delta\nu \delta t}} [\text{Jy}] \quad (3.3)$$

Where  $T_{\text{sys}}$  is the system temperature,  $A_{\text{eff}}$  is the effective area of the antenna/station,  $k_B$  is the Boltzmann constant,  $\delta\nu$  is the frequency resolution and  $\delta t$  is the integration time of the visibilities. The  $A_{\text{eff}}/T_{\text{sys}}$ <sup>6</sup> values for SKA1-Low are listed by Braun et al. [53]. We interpolated the  $A_{\text{eff}}/T_{\text{sys}}$  values to the frequencies of interest. For this case, we assume the residual foreground contaminations are below the H<sub>I</sub> signal level. The only contamination present in the H<sub>I</sub> maps is thermal noise. The contribution of the thermal noise in the visibility domain is rescaled by the factor of  $\sqrt{t_{\text{obs}}/t_{\text{obs}}^{\text{uv}}}$ , where  $t_{\text{obs}}^{\text{uv}} = 0.5$  h represents the observation time per day will be restricted to  $\pm 0.15$  minutes around the transit time of the target EoR field and  $t_{\text{obs}}$  is the total integration time. This rescaling represents the coherent averaging of

<sup>6</sup>[https://www.skao.int/sites/default/files/documents/SKAO-TEL-0000818-V2\\_SKA1\\_Science\\_Performance.pdf](https://www.skao.int/sites/default/files/documents/SKAO-TEL-0000818-V2_SKA1_Science_Performance.pdf)

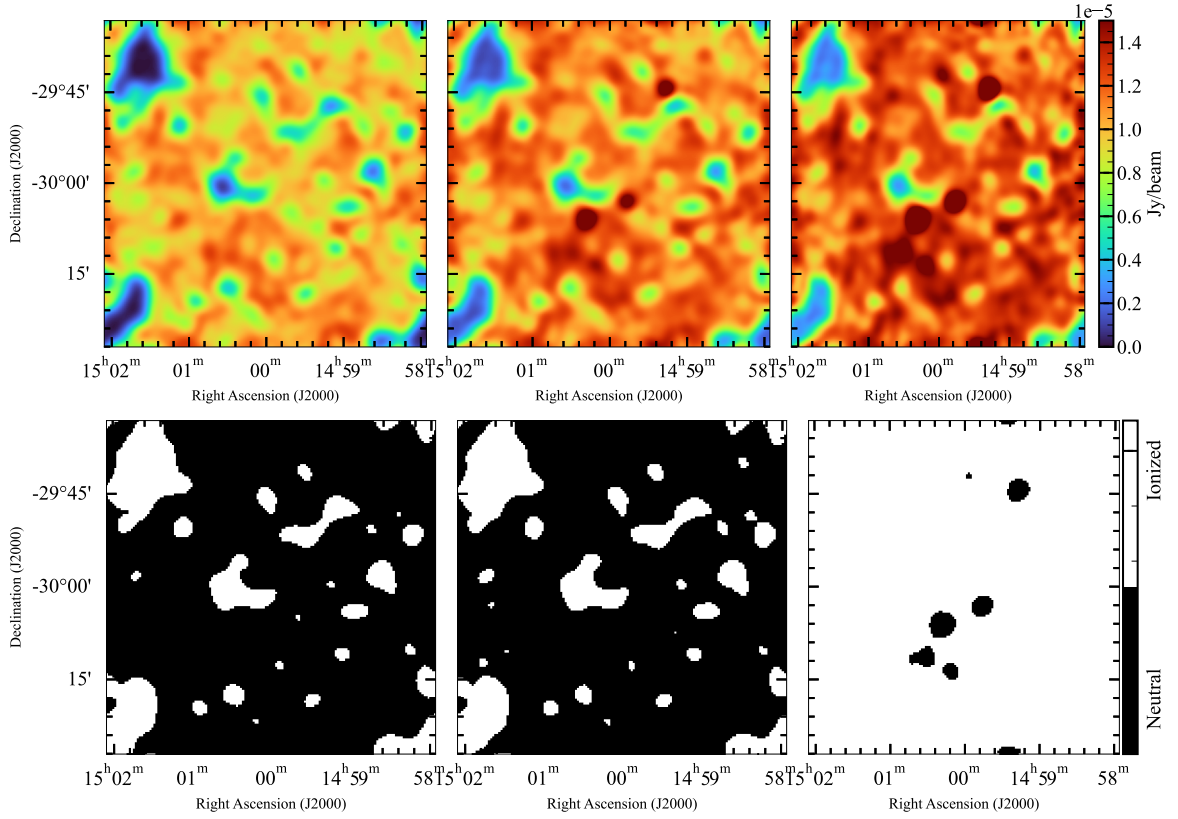


**Figure 3:** An example of a slice through the sky plane used during the LCS analysis. Top Left : The observed H<sub>I</sub> 21 cm brightness temperature fields of  $\bar{x}_{\text{HI}} \approx 0.55$  from the 21cmE2E-pipeline. Top Middle: The residual fields after incorporating calibration error  $\sim 0.05\%$ . Top Right: The residual fields after incorporating calibration error  $\sim 0.09\%$ . It is seen that higher calibration errors reduce the dynamic range of the H<sub>I</sub> maps, making it more challenging to mask ionized bubbles and accurately binarize the H<sub>I</sub> maps. Bottom: The recovered H<sub>II</sub> regions after applying the triangle method. With a calibration error of  $\sim 0.09\%$ , the thresholding algorithm failed to binarize the residual fields. The white (black) regions represent the recovered H<sub>II</sub> and H<sub>I</sub> regions.

visibility data over the total integration time. For this simulation, we vary the total integration time of 1000, 1500, and 2000<sup>7</sup> to achieve a good signal-to-noise ratio level ( $\text{SNR} \gtrsim 3$ ) in the synthesized map.

To incorporate the thermal noise into the simulation, we downsampled the simulated 21 cm maps by a factor of 16 along each side. As discussed in our previous study, the synthetic 21 cm observations require input maps with dimensions of  $2^{3n}$  grids. We used a downsampling

<sup>7</sup>Our simulations track the sky for only 30 minutes per observation for computational efficiency. To accumulate 2000 hours of observation time, this requires 4000 repetitions. In contrast, actual observations with a 4 hour daily tracking time would necessitate 500 repetitions of the same sky patch, taking approximately two years to achieve the desired observation time. If we shift the phase centre a bit of arcsec, we can mitigate the systematics effect.

algorithm available in the PYTHON package SCIKIT-IMAGE and integrated this method into the 21cmE2E pipeline. This downsampling is essential to reduce the total observation time to achieve the desired SNR level. After downsampling the maps, the grid size of the final maps is 8.96 cMpc for redshift  $z = 7.48$ , which corresponds to an angular resolution of 3.42 arcmin and a frequency resolution of 0.54 MHz. We generated the image cubes using the 21cmE2E pipeline after adding the thermal noise. In order to balance the resolution and the sensitivity of the telescope, two different imaging weighting schemes are used: natural weighting and briggs weighting. The natural weighting scheme provides a relatively higher SNR but a lower resolution compared to the briggs weighting scheme with a robust parameter of 0.5. The left and middle panel of Figure 4 shows the slices of the brightness temperature field before and after adding the thermal noise with an observation time of 2000 h at a channel width of 0.54 MHz, respectively, at neutral fraction  $\bar{x}_{\text{HI}} = 0.39$  ( $z = 7.48$ ). It is seen that more tunnel-like artefacts are visible on the map after introducing thermal noise. These artefacts result from the effect of noise and deconvolution. In the later section 5.3, we discuss how this feature will affect the percolation process. The right panel of Figure 4 shows the recovered HII regions after applying an entropy-based thresholding algorithm (Yen’s method). In this map, white regions represent recovered HII regions, while black regions represent HI regions.

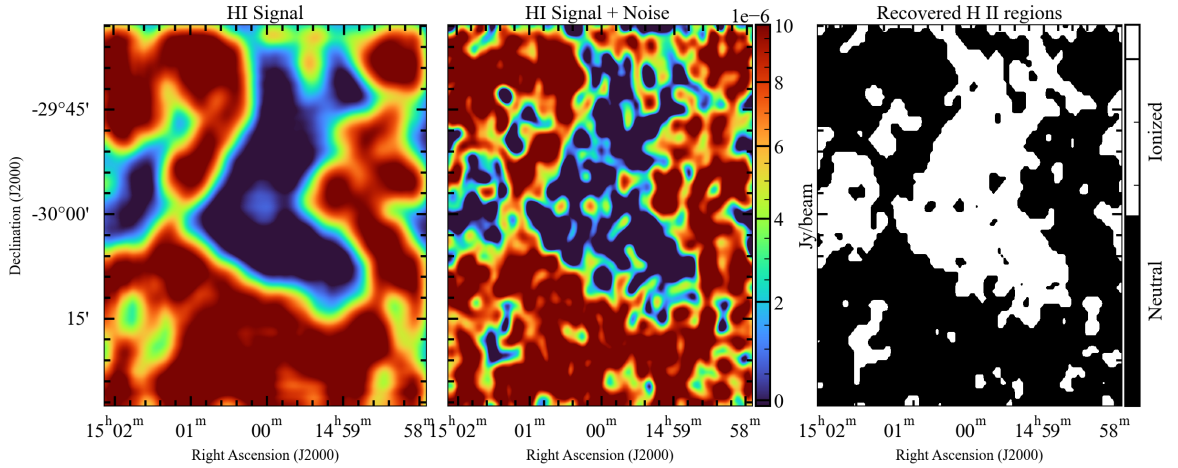


**Figure 4:** The pictorial representation of HI maps of  $\bar{x}_{\text{HI}} = 0.39$  after performing multiscale cleaning with the natural weighting scheme through the 21cmE2E-pipeline. Left: The observed HI field without adding noise. Middle: Instrumental noise added to the HI 21 cm field for an observation time of 2000 hours when observed with SKA1-Low with 296 stations. Right: Identified ionized region from the 21 cm field after applying entropy-based thresholding algorithm (Yen’s method). The black (white) regions represent the ionized (neutral) regions in the HI 21 cm field.

## 4 Percolation Transition & LCS

In this section, we discuss a probe for the percolation process called the Largest Cluster Statistics (LCS) [54–56]. In the early stage of reionization, a small group of ionized regions is formed, and the size and number of the ionized region grow gradually with time. At

some point in time, these isolated ionized regions abruptly merge together to form a singly connected large ionized region spanning the entire IGM. This phase transition of the ionized region is known as the percolation transition [57, 58]. With the help of LCS, we draw inferences on the percolation process, especially on the percolation transition point. We identify the percolation transition occurring when the largest ionized region (LIR) spans the entire simulated volume and becomes formally infinitely extended owing to the periodic boundary conditions. In this work, which is a follow-up of a [29, 30, 32, 33], we follow the evolution of the large ionized region as reionization advances using LCS. The LCS is defined as

$$\text{LCS} = \frac{\text{volume of the largest ionized region}}{\text{total volume of all the ionized regions}} \quad (4.1)$$

As can be seen from the above definition, LCS represents the fraction of ionized volume residing within the LIR. Hence, at the onset of the percolation transition, an abrupt increase in LCS is anticipated. This abrupt transition defines the percolation transition threshold. We plot LCS as a function of the mass-averaged neutral fraction ( $\bar{x}_{\text{HI}}$ ), e.g. in Figure 6, to characterize the evolution of the LIR as the neutral fraction decays with reionization. The critical  $\bar{x}_{\text{HI}}$  denotes the threshold at which percolation transition occurs, where small ionized regions merge into a large ionized region spanning the entire IGM. The sudden increase in LIR volume results in a sharp increase in the LCS. We identify the percolation transition threshold as the point at which the change in LCS is the maximum. Therefore, both the LCS profile and its critical value at the percolation transition serve as crucial metrics for evaluating the morphological evolution and history of reionization. Previous works by [29, 30, 32, 33] have shown that the LCS can be a good metric to probe the percolation process and thereby distinguish extreme models of reionization. Our study focuses on the evolution of LCS from the coeval boxes observed through synthetic 21 cm observations with SKA1-Low. In real observation, we observed the light-cone effect [59]. However, its impact on the evolution of the LCS along a line-of-sight has minimal (Potluri et al., in prep). We use coeval boxes to study the evolution of LCS from 21 cm observation. Therefore, the effect of light-cone is not expected to be so dominant and is beyond the scope of this paper.

#### 4.1 Binarization of the image cubes

In order to estimate the LCS on the brightness temperature maps, we use a code, SURFGEN2 [29, 30, 60, 61]. SURFGEN2 not only determines the LCS but also helps identify the topological and morphological features of each ionized region using Shapefinders [62].<sup>8</sup> For an in-depth understanding of the operating principles of the SURFGEN2 code, readers can refer to [30, 61]. The SURFGEN2 code requires thresholding to binarize the neutral and ionized regions of the H<sub>I</sub> maps. In an ideal H<sub>I</sub> 21 cm brightness temperature field ( $\delta T_b$ ), an ionized region is identified by  $\delta T_b$  equal to zero. For an interferometric observation, we measure only the fluctuations in the 21 cm signal. Accordingly, the minima of the brightness temperature maps correspond to ionized regions, as expected. However, in real observations, the presence of systematic effects poses a challenge in finding the optimal

---

<sup>8</sup>Shapefinders are derived from the ratios of the Minkowski functionals. For instance, in three dimensions, the four Minkowski functionals give rise to three shapefinders, with each one representing the extent of a closed surface along one of the three dimensions; see [62] for more details.



threshold to distinguish the ionized regions. In our previous work, Dasgupta et al. [33], imposed a gradient-descent method on the histograms of the synthetically observed  $H_{\text{I}}$  maps by the SKA1-Low to binarize them. When we add calibration errors and instrumental noise to the  $H_{\text{I}}$  maps, finding an optimal threshold becomes a challenging task. In this paper, we employ the intensity-based thresholding algorithm (i.e., triangle method [63, 64]) for calibration errors and the entropy-based thresholding algorithm (i.e., Yen’s method) [64, 65] for instrumental noise to separate image pixels. In future work, we will investigate the optimal thresholding for binarizing the  $H_{\text{I}}$  field from interferometric observations (Dasgupta et. al., in prep).

## 5 Results

This section discusses the impact of the thresholding method, antenna-based calibration errors and the instrumental noise for SKA1-Low on LCS analyses. We use the 21cmE2E pipeline to assess how each of these factors affects the percolation process during different stages of reionization. The following subsections present detailed results for each factor considered.

### 5.1 Effect of thresholding

This work presents an optimum strategy to reduce the bias in LCS estimation from the simulated 21 cm observation results. Our previous study, Dasgupta et al. [33] used a thresholding method, e.g., gradient descent, to binarize 21 cm maps and estimate the LCS. During the early stages of reionization, the histogram of 21 cm maps is not bimodal. Instead, it exhibits an unimodal distribution with asymmetric tails, as indicated by non-zero skewness [34, 66]. This thresholding method introduces bias for these cases due to its limitations in reaching the local minima in the 21 cm observation maps. The problem becomes more significant when telescope effects, such as the proper implementation of the array synthesized beam of SKA1-Low, are included. Therefore, these limitations fail to binarize the image pixels and lead to biases in the recovered percolation process of reionization. In order to mitigate these challenges, we use the triangle method to separate the neutral and ionized regions. This method identifies the threshold by drawing a line from the peak of the histogram to the end of the asymmetric tail and determining the point of maximum distance between this line and the histogram. The visual representation of the triangle method is shown in Figure 5. This method effectively separates ionized and neutral regions during different stages of EoR from the noiseless data [67]. In Figure 6, we compare the estimation of LCS obtained from the simulated 21 cm observation against neutral fraction using different thresholding methods. The original image is a hypothetical scenario without telescope effect and noise, and the corresponding threshold for LCS is set at zero. The red dash-dot and green dashed curves represent the estimation of LCS based on the thresholds obtained via the triangle and gradient-descent methods, respectively. The triangle method demonstrates superior performance compared to the gradient-descent method. We observe that the threshold set by the triangle method on the simulated 21 cm observations results in the same percolation transition redshift or  $\bar{x}_{\text{HI}} \approx 0.7$  [29, 32–34, 36] as that of the hypothetical scenario, i.e. without any telescope effect and noise shown by the blue solid curve. However, the obtained LCS

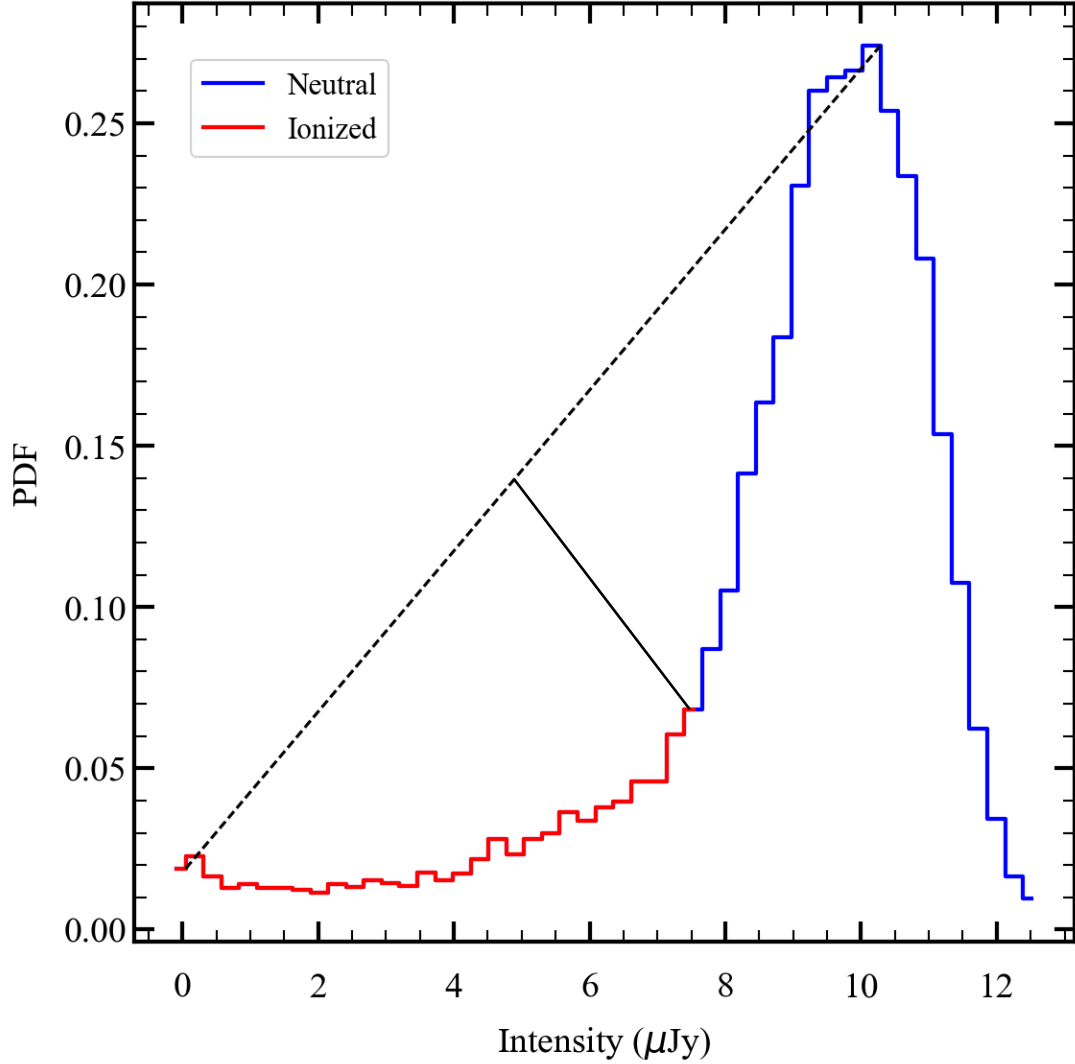


**Figure 5:** The pictorial representation of the triangle method. The triangle method is an automated image-thresholding technique that determines the optimal threshold value from an image histogram. This method identifies the threshold by drawing a line from the peak of the histogram to the end of the asymmetric tail and determining the maximum point of the distance between this line and the histogram. When the bimodal feature of the histogram of the 21 cm field is not clearly defined, it displays an unimodal distribution with an asymmetric tail. In such cases, the triangle method, as a global thresholding technique, effectively locates local minima in the 21 cm maps. The resulting segmentation distinguishes between neutral and ionized regions, as indicated by the different colours in the histogram.

based on the threshold set by the triangle method has small deviations from the original LCS estimation, which is due to the resolution of the telescope and the error in the thresholding method.

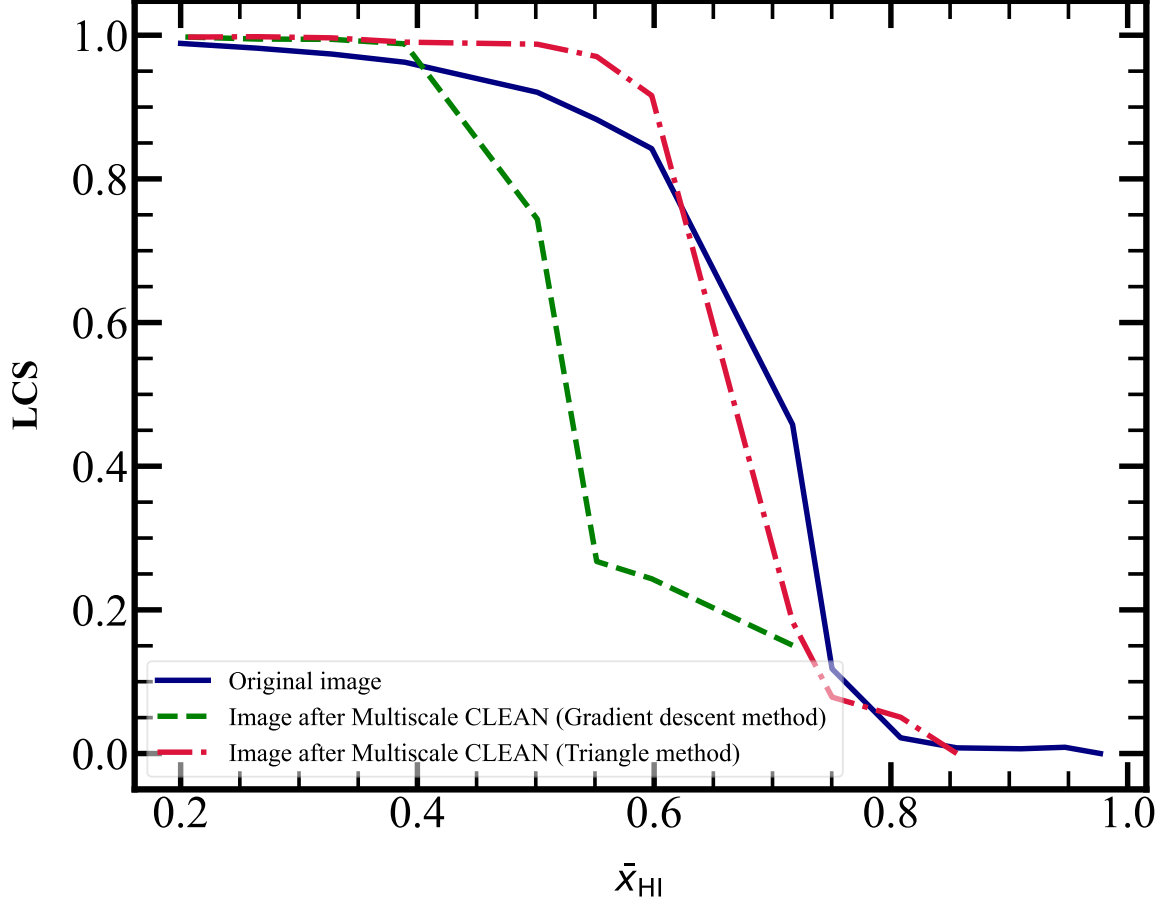


**Figure 6:** Comparison of estimated LCS against neutral fraction using different thresholding algorithms. The original image is a hypothetical scenario without telescope effect and noise, and the corresponding threshold for LCS is set at zero. The red dash-dot and green dashed curve represent the estimation of LCS based on the thresholds obtained via the triangle and gradient-descent methods. The triangle method demonstrates superior performance compared to the gradient-descent method. We observe that the threshold set by the triangle method on the simulated 21 cm observations results in the same percolation transition redshift or  $\bar{x}_{\text{HI}} \approx 0.7$  as that of the hypothetical scenario, i.e. without any telescope effect and noise shown by the blue solid curve.

## 5.2 Effect of gain calibration error

This section investigates the impact of antenna-based gain calibration errors on the obtained LCS from synthetic 21 cm observations with SKA1-Low. The analysis is based on the threshold set via the triangle method on residual image cubes. There are many techniques that have been developed to remove residual contamination from the image domain [4].



However, we aim to determine the maximum tolerance level of antenna-based calibration error to recover the reionization history in a robust and relatively unbiased manner using LCS. We varied antenna-based calibration errors to estimate this tolerance level to achieve a sufficient dynamic range to extract the 21 cm signal from residual data. Here, two types of foreground corruption conditions were considered, as discussed in [subsection 2.2](#). We discuss the results obtained for the different cases of foreground models below.

**Case I:** Figure 7 shows the evolution of obtained LCS against  $\bar{x}_{\text{HI}}$  for varying levels of calibration errors in the sky models for Case I. These residual data consist of residual

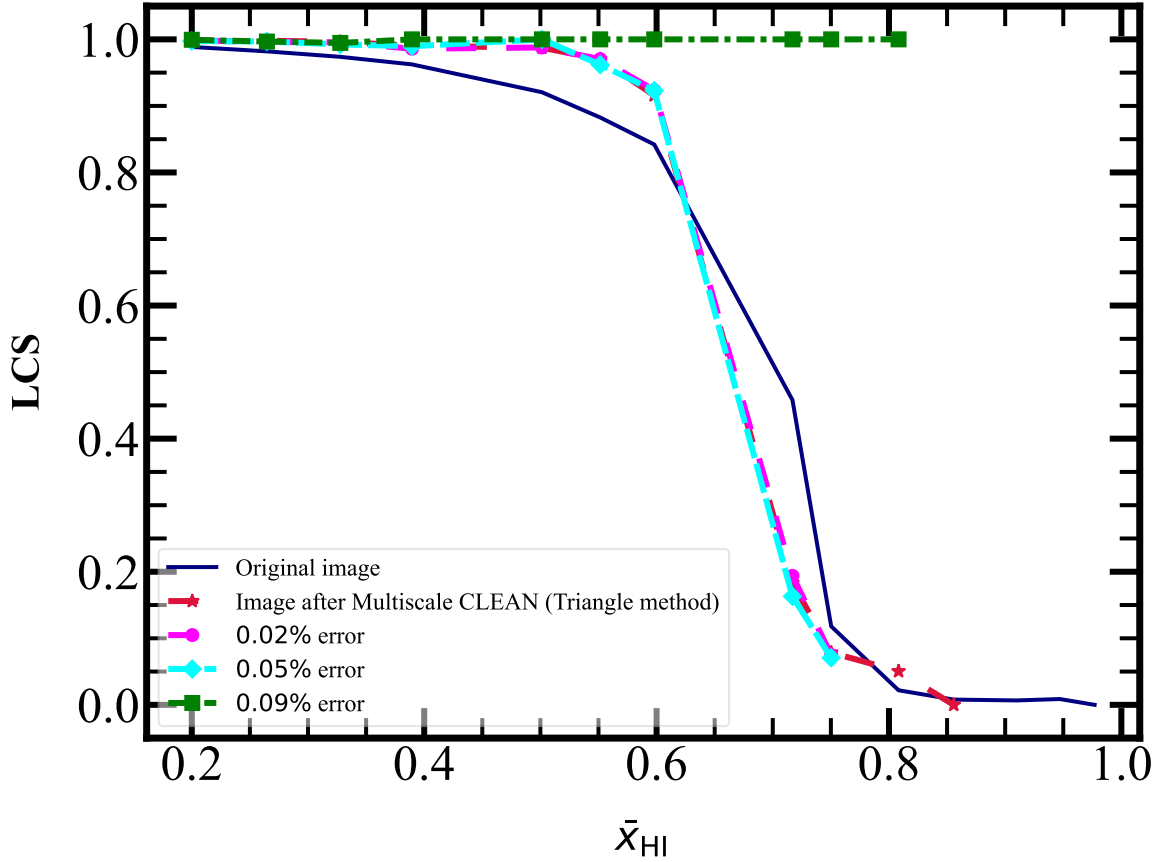


**Figure 7:** The LCS is computed as a function of neutral fraction  $\bar{x}_{\text{HI}}$  for varying levels of gain calibration errors, focusing solely on point sources in Case I. The original image is a hypothetical scenario without telescope effect and noise, and the corresponding threshold for LCS is set at zero. The magenta circle, cyan diamond, and green square curves represent the estimated LCS based on the threshold obtained via the triangle method for different post-gain calibration errors of 0.02%, 0.05%, and 0.09%, respectively. We observed that the obtained LCS for calibration errors up to 0.05% follow the threshold set by the triangle method on the simulated 21 cm observations results without the calibration errors shown by the red dashed curve. With a higher calibration error, the thresholding method failed to binarize the image pixels, introducing bias on the LCS analysis indicated by the green square curve.

point sources and the target signal. The blue solid curve represents the original image, a hypothetical scenario without telescope effect and noise, and the corresponding threshold for LCS is set at zero. The magenta circle, cyan diamond, and green square curves represent the obtained LCS from simulated 21 cm observation via 21cmE2E pipeline based on the threshold set by the triangle method for different post-gain calibration errors of 0.02%, 0.05%, and 0.09%, respectively. We observed that obtained LCS from simulated 21 cm observations with calibration errors up to 0.05% follow with the obtained LCS without any bias due to corruption, as shown by the red star curve. However, beyond a calibration inaccuracy of 0.09%, the computation of LCS becomes challenging. At this level, RMS noise overwhelms the image pixels, and the imperfect removal of foreground residuals significantly impacts the bimodal distribution of simulated 21 cm maps. This corruption makes it challenging to separate ionized and neutral regions accurately. At higher calibration errors, this thresholding method fails to recover ionized regions due to biases in the histogram of the bimodal distribution. This thresholding method misidentified unsubtracted residual contamination as neutral regions and other regions as ionized regions, as shown in the bottom-right panel of Figure 3. Therefore, the SURFGN2 code provides the value of LCS close to unity, as indicated by the green square line in Figure 7.

**Case II:** Figure 8 shows the evolution of LCS against  $\bar{x}_{\text{HI}}$  for different levels of calibration errors in the sky models for Case II. The sky models consist of residual point sources, diffuse emission, and the target signal. The magenta circle, cyan diamond, and green square curves represent the obtained LCS from simulated 21 cm observation via 21cmE2E pipeline based on the threshold set by the triangle method for different post-gain calibration errors of 0.02%, 0.05%, and 0.09%, respectively. We observed that obtained LCS from simulated 21 cm observations with calibration errors up to 0.05% follow with the obtained LCS without any bias due to corruption, as shown by the red star curve. However, with calibration inaccuracy of  $\sim 0.09\%$ , the computation of LCS becomes challenging as residual foreground contamination starts to dominate the image and introduces bias in LCS analysis. A similar effect of gain calibration errors on the obtained LCS from simulated 21 cm observations is observed across both groups of foreground models.

We observed that calibration errors introduce artificial filamentary or tunnel-like features (deconvolution artefacts) in the final image cube. These artefacts fragment the largest ionized region into isolated regions. The fragmentation depends on the thresholding method used to separate the H<sub>I</sub> field. The left panel of Figure 8 highlights the impact of these deconvolution artefacts, such as artificial filamentary or tunnel-like features, on the LCS analysis, particularly in the dip scenario. It is essential to note that imperfect subtraction of bright sources can also create a negative bowl-like region. These regions further fragment the largest ionized region into pieces, introducing additional bias in the LCS analysis. Our initial systematic study emphasizes the critical importance of achieving calibration accuracy for the upcoming SKA1-Low observations. Such accuracy is essential to recover the reionization history in a robust and unbiased manner using the LCS. However, the choice of thresholding algorithm significantly impacts the LCS analysis. Future work will explore different thresholding algorithms to improve the separation of neutral and ionized regions during LCS estimation.

### 5.3 Effect of instrumental noise

Figure 10 shows the evolution of obtained LCS from 21 cm observation against  $\bar{x}_{\text{HI}}$  for different observation times and imaging weighting. For deep 21 cm observations with 1500 hours and 2000 hours of integration time, the obtained LCS up to  $\bar{x}_{\text{HI}} \sim 0.6$ , threshold set by Yen's method shown by magenta square and black cross curves, respectively consistent with the estimation of LCS from the original downsampled image cube, represented by a red dotted curve. The choice of weighting scheme significantly affects the properties of synthesized

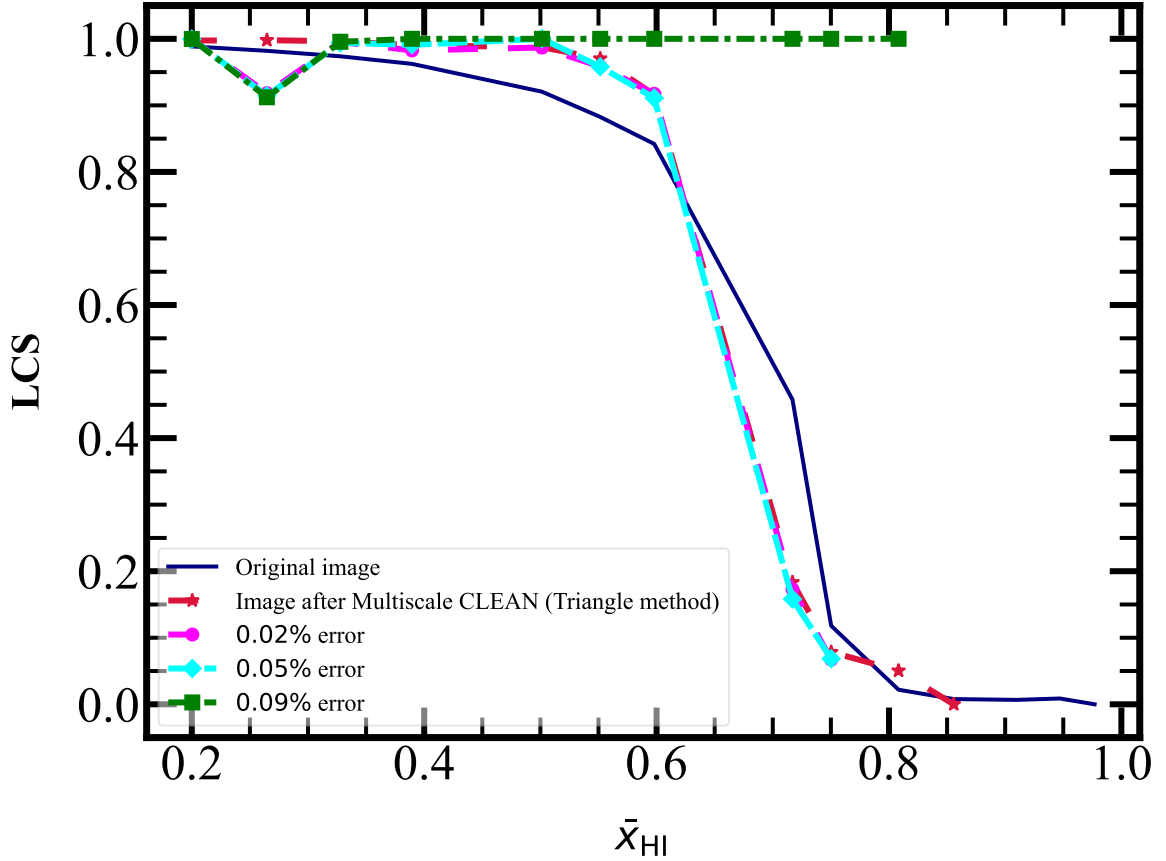


**Figure 8:** The LCS is computed as a function of neutral fraction  $\bar{x}_{\text{HI}}$  for varying levels of gain calibration errors, focusing on realistic foreground models in Case II. The original image is a hypothetical scenario without telescope effect and noise, and the corresponding threshold for LCS is set at zero. The magenta circle, cyan diamond, and green square curves represent the obtained LCS from simulated 21 cm observations based on the threshold set by the triangle method for different post-gain calibration errors of 0.02%, 0.05%, and 0.09%, respectively. We observed that the obtained LCS for calibration errors up to 0.05% follow the threshold set by the triangle method on the simulated 21 cm observations without any corruption result shown by the red star curve. With a higher calibration error, the thresholding method failed to binarize the image pixels, introducing bias on the LCS analysis indicated by the green square line.

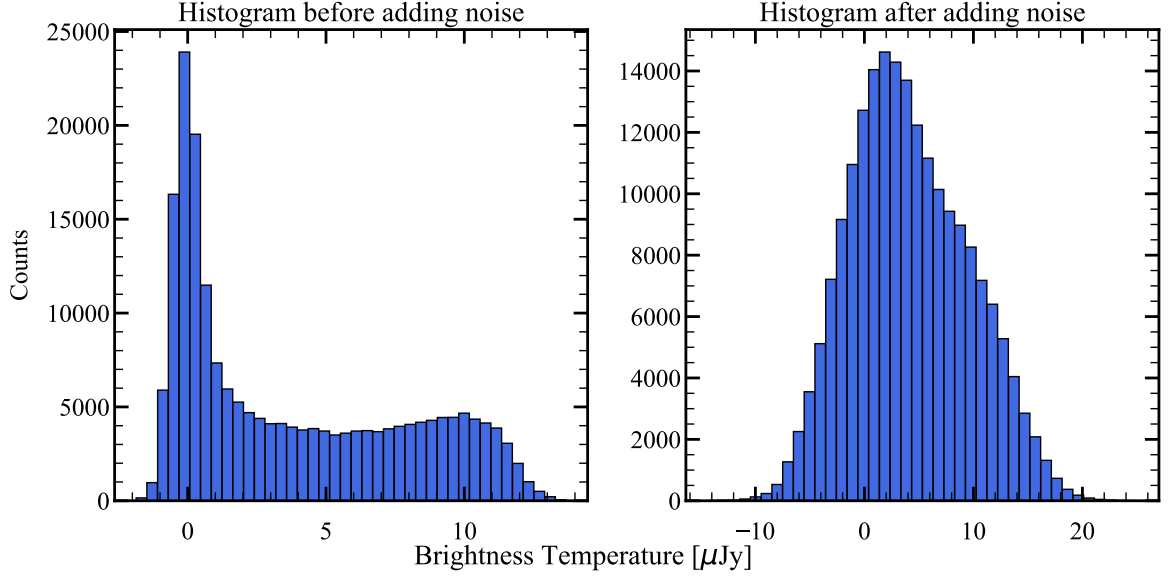


**Figure 9:** The variation in the histogram of bimodal distributions of 21 cm field at a fixed neutral fraction before (left panel) and after (right panel) adding the instrumental noise of SKA1-Low telescope. Introducing random fluctuations in the simulated 21 cm observation results in the loss of bimodality and shifts the histogram towards a Gaussian distribution. These random fluctuations shift the pixel intensities in the 21 cm field by random values, leading to a bias in threshold identification using the triangle method.

image cubes. With the natural weighting scheme, the resolution of the synthesized image cubes is relatively lower than that of the briggs weighting scheme. However, it offers a higher signal-to-noise ratio (SNR) in the final maps than briggs weighting. After adding instrumental noise, small-scale filamentary structures appear in the image cubes. In the natural weighting scheme, larger ionized regions contribute to LCS estimation due to lower resolution and higher SNR. In contrast, in the briggs weighting scheme, the poorer SNR causes numerous small filamentary structures that may be classified as either ionized or neutral, depending on the thresholding algorithm. Thus, the choice of the weighting scheme affects the synthesized maps, which in turn impacts the obtained LCS from the 21 cm observation. We observed that the features of the obtained LCS could be computed up to a certain neutral fraction  $\bar{x}_{\text{HI}}$ , and the percolation transition point shifts significantly toward lower redshifts. This shift is caused by the combined effects of the instrumental noise and the partially ionized regions in the H<sub>21</sub> cm field. Thus, this leads to a biased interpretation of the history of reionization. Our findings highlight the significance of imaging weighting to obtain the LCS from 21 cm observation. In addition, it emphasized the importance of the thresholding algorithm to separate neutral and ionized pixels in noisy data and the impact of cluster detection within the SURFGEN2 code on LCS estimation. Future work will explore alternative thresholding algorithms for improved pixel differentiation.

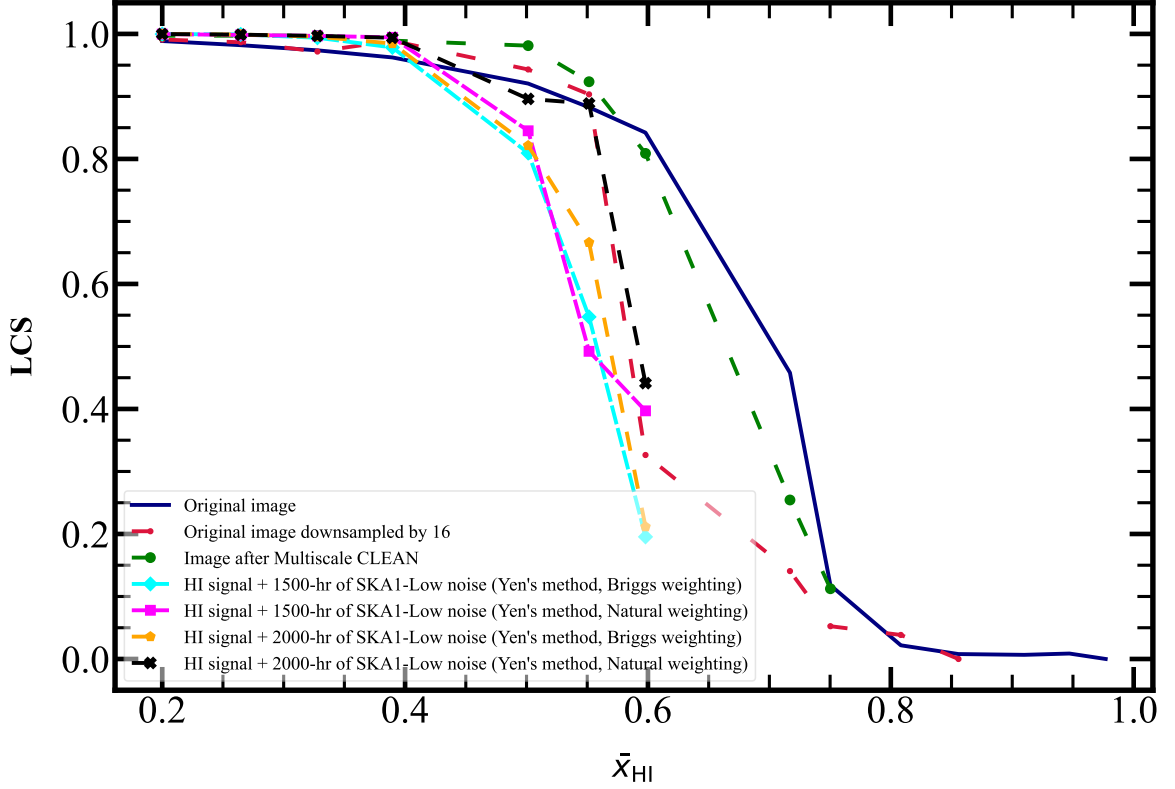


**Figure 10:** The LCS is computed as a function of neutral fraction  $\bar{x}_{\text{HI}}$  for varying levels of accumulated time of observations and different types of imaging weighting schemes. The original image is a hypothetical scenario without telescope effect and noise, and the corresponding threshold for LCS is set at zero, indicated by a blue solid curve. A red dotted curve indicates the original downsampled image, based on the threshold set by the triangle method. For deep 21 cm observations with 1500 hours and 2000 hours of integration time, the obtained LCS up to  $\bar{x}_{\text{HI}} \sim 0.6$ , threshold set by Yen’s method shown by the magenta circle and black cross curves, respectively consistent with the estimation of LCS from the original downsampled image cube. At the higher neutral fraction, the LCS cannot be computed because of random fluctuations dominating the 21 cm field.

## 6 Summary and discussion

This work investigated the effect of antenna-based calibration errors and instrumental noise for SKA1-Low on LCS analysis. We aim to recover the reionization history using the LCS in a robust and relatively unbiased manner. The key findings of this investigation are summarized as follows:

- The histogram of the brightness temperature map of the 21 cm field during EoR exhibits a bimodal distribution. The two peaks correspond to ionized and neutral regions. In a hypothetical scenario without telescope effects or noise, ionized regions would have a brightness temperature of zero. However, in radio interferometric observation, determining an optimal threshold to distinguish neutral from ionized regions in the

21 cm brightness map is challenging. The complexity arises from the systematic effects, resolution of the telescope, and thermal noise, which cause random shifts in pixel brightness temperature maps. Therefore, accurately differentiating between these regions in 21 cm maps becomes difficult. In this study, we present alternative thresholding strategies to binarize the image pixels to recover the percolation transition. It was observed that the bias of estimation of LCS of the 21 cm maps reduces after employing the triangle method of thresholding. Furthermore, we observed that the threshold set by the triangle method on the simulated 21 cm observations results in the same percolation transition redshift or  $\bar{x}_{\text{HI}} \approx 0.7$  as a hypothetical scenario, i.e. without any telescope effect and noise. However, the obtained LCS has a little deviation from the actual LCS estimation from the hypothetical scenario due to the resolution of the SKA1-Low telescope.

- We study the effect of direction-independent calibration errors on the percolation process of reionization history using the LCS of the 21 cm maps. We have demonstrated that a post-calibration and post-averaging antenna-based calibration error tolerance of  $\sim 0.05\%$  is essential to achieve unbiased and unaffected LCS estimation. This corresponds to an amplitude error of  $\sim 0.05\%$  and a phase error of  $\sim 0.05^\circ$  in each time domain. It is important to note that the tolerance of  $\sim 0.05\%$  will vary depending on the RMS variation across different sky patches, i.e., the statistical distribution of bright sources within the FoV. We also observed that the threshold set by the triangle method on the residual 21 cm maps simulated via 21cmE2E aligns with the same percolation transition redshift or  $\bar{x}_{\text{HI}} \approx 0.7$ , as results from the simulated 21 cm observations without any bias due to corruption. However, at higher calibration errors ( $\sim 0.09\%$ ), the dynamic range of the 21 cm maps deteriorates. The RMS noise from the residual foreground starts to dominate the image pixels and affects the sharp features of the bimodal distribution of the H<sub>I</sub> 21 cm field. Under these conditions, the thresholding method, e.g. the triangle method, struggles to distinguish neutral and ionized regions. This results in a biased estimation of LCS.
- The calibration errors introduce artefacts, such as artificial filament structures, in the observed H<sub>I</sub> maps during deconvolution. When the thresholding algorithm is used to binarize the image pixels, these artefacts cause the largest ionized region to fragment into isolated segments, thereby introducing dips in the LCS evolution for low  $\bar{x}_{\text{HI}}$ . The peeling of bright sources can further break down the largest ionized regions. This fragmentation depends on the spatial distribution of the point sources.
- Next, we introduce the instrumental noise for SKA1-Low to assess the robustness of the evolution of the obtained LCS. After introducing the instrumental noise, it is observed that the bimodal feature of the 21 cm map is lost, and the histogram shifts towards a Gaussian distribution. Our initial analysis used the triangle method to binarize the image pixels. However, it later proved to be inadequate for determining an optimal threshold, resulting in inaccurate percolation analysis during reionization. To address this, we used an entropy-based thresholding algorithm, Yen's method. This method determined the optimal threshold for minimizing the entropy of the pixel intensity

distribution. We observed that with an accumulation of 2000 h of observation time, the estimation of the LCS threshold set by Yen’s method remains unchanged and unbiased from the results of the estimation of LCS from the original downsampled image cubes. This accumulation of observation time represents an optimistic test for the robustness of LCS under realistic conditions. However, during the early stages of reionization, i.e., at the higher neutral fractions, the feature of LCS is lost owing to random fluctuations in the thermal noise that dominate the ionization fluctuations. Furthermore, for total observation periods smaller than 1500 hours, the lower SNR significantly limits the computation of the estimation LCS from 21 cm observation. As the contrast between ionized bubbles and random fluctuations becomes comparable, the performance of the LCS analysis is impacted.

We demonstrate that the obtained LCS results can be biased depending on the choice of thresholding method. Therefore, the development of a robust thresholding method is essential for precise percolation analysis across all reionization stages. However, we should have accounted for the impact of ionospheric phase distortion, the chromatic nature of the primary beam, and other systematic problems. These factors could further complicate the LCS analysis. Our future work will address these factors to provide a more comprehensive understanding of their implications for EoR 21 cm, and subsequent LCS analysis.

## 7 Acknowledgements

SKP acknowledges the financial support by the Department of Science and Technology, Government of India, through the INSPIRE Fellowship [IF200312]. The authors acknowledge the use of facilities procured through the funding via the Department of Science and Technology, Government of India sponsored DST-FIST grant no. SR/FST/PSII/2021/162 (C) awarded to the DAASE, IIT Indore. AD and SM acknowledge financial support through the project titled “Observing the Cosmic Dawn in Multicolour using Next Generation Telescopes” funded by the Science and Engineering Research Board (SERB), Department of Science and Technology, Government of India through the Core Research Grant No. CRG/2021/004025. SB acknowledges the funding provided by the Alexander von Humboldt Foundation. SB thanks Varun Sahni and Santanu Das for their contributions to the development of SURFGEN2.

## References

- [1] X. Fan, C.L. Carilli and B. Keating, *Observational Constraints on Cosmic Reionization*, *Ann. Rev. Astron. Astrophys.* **44** (2006) 415 [[astro-ph/0602375](#)].
- [2] G. Paciga, J.G. Albert, K. Bandura, T.-C. Chang, Y. Gupta, C. Hirata et al., *A simulation-calibrated limit on the H I power spectrum from the GMRT Epoch of Reionization experiment*, *Mon. Not. Roy. Astron. Soc.* **433** (2013) 639 [[1301.5906](#)].
- [3] M. Kolopanis, J.C. Pober, D.C. Jacobs and S. McGraw, *New EoR power spectrum limits from MWA Phase II using the delay spectrum method and novel systematic rejection*, *Mon. Not. Roy. Astron. Soc.* **521** (2023) 5120 [[2210.10885](#)].



- [4] F.G. Mertens, M. Mevius, L.V.E. Koopmans, A.R. Offringa, G. Mellema, S. Zaroubi et al., *Improved upper limits on the 21 cm signal power spectrum of neutral hydrogen at  $z \approx 9.1$  from LOFAR*, *Mon. Not. Roy. Astron. Soc.* **493** (2020) 1662 [[2002.07196](#)].
- [5] HERA Collaboration, Z. Abdurashidova, T. Adams, J.E. Aguirre, P. Alexander, Z.S. Ali et al., *Improved Constraints on the 21 cm EoR Power Spectrum and the X-Ray Heating of the IGM with HERA Phase I Observations*, *Astrophys. J.* **945** (2023) 124.
- [6] S. Bharadwaj and S.S. Ali, *On using visibility correlations to probe the HI distribution from the dark ages to the present epoch - I. Formalism and the expected signal*, *Mon. Not. Roy. Astron. Soc.* **356** (2005) 1519 [[astro-ph/0406676](#)].
- [7] V. Jelić, S. Zaroubi, P. Labropoulos, R.M. Thomas, G. Bernardi, M.A. Brentjens et al., *Foreground simulations for the LOFAR-epoch of reionization experiment*, *Mon. Not. Roy. Astron. Soc.* **389** (2008) 1319 [[0804.1130](#)].
- [8] V. Jelić, S. Zaroubi, P. Labropoulos, G. Bernardi, A.G. de Bruyn and L.V.E. Koopmans, *Realistic simulations of the Galactic polarized foreground: consequences for 21-cm reionization detection experiments*, *Mon. Not. Roy. Astron. Soc.* **409** (2010) 1647 [[1007.4135](#)].
- [9] O. Zahn, A. Mesinger, M. McQuinn, H. Trac, R. Cen and L.E. Hernquist, *Comparison of reionization models: radiative transfer simulations and approximate, seminumeric models*, *Mon. Not. Roy. Astron. Soc.* **414** (2011) 727 [[1003.3455](#)].
- [10] S. Choudhuri, S. Bharadwaj, S.S. Ali, N. Roy, H.T. Intema and A. Ghosh, *The angular power spectrum measurement of the Galactic synchrotron emission in two fields of the TGSS survey*, *Mon. Not. Roy. Astron. Soc.* **470** (2017) L11 [[1704.08642](#)].
- [11] A. Chakraborty, N. Roy, A. Datta, S. Choudhuri, K.K. Datta, P. Dutta et al., *Detailed study of ELAIS N1 field with the uGMRT - II. Source properties and spectral variation of foreground power spectrum from 300-500 MHz observations*, *Mon. Not. Roy. Astron. Soc.* **490** (2019) 243 [[1908.10380](#)].
- [12] A. Mazumder, A. Chakraborty, A. Datta, S. Choudhuri, N. Roy, Y. Wadadekar et al., *Characterizing EoR foregrounds: a study of the Lockman Hole region at 325 MHz*, *Mon. Not. Roy. Astron. Soc.* **495** (2020) 4071 [[2005.05205](#)].
- [13] N. Barry, B. Hazelton, I. Sullivan, M.F. Morales and J.C. Pober, *Calibration requirements for detecting the 21 cm epoch of reionization power spectrum and implications for the SKA*, *Mon. Not. Roy. Astron. Soc.* **461** (2016) 3135 [[1603.00607](#)].
- [14] A.H. Patil, S. Yatawatta, S. Zaroubi, L.V.E. Koopmans, A.G. de Bruyn, V. Jelić et al., *Systematic biases in low-frequency radio interferometric data due to calibration: the LOFAR-EoR case*, *Mon. Not. Roy. Astron. Soc.* **463** (2016) 4317 [[1605.07619](#)].
- [15] A. Ewall-Wice, J.S. Dillon, A. Liu and J. Hewitt, *The impact of modelling errors on interferometer calibration for 21 cm power spectra*, *Mon. Not. Roy. Astron. Soc.* **470** (2017) 1849 [[1610.02689](#)].
- [16] A. Mazumder, A. Datta, A. Chakraborty and S. Majumdar, *Observing the reionization: effect of calibration and position errors on realistic observation conditions*, *Mon. Not. Roy. Astron. Soc.* **515** (2022) 4020 [[2207.06169](#)].
- [17] C.H. Jordan, S. Murray, C.M. Trott, R.B. Wayth, D.A. Mitchell, M. Rahimi et al.,



*Characterization of the ionosphere above the Murchison Radio Observatory using the Murchison Widefield Array*, *Mon. Not. Roy. Astron. Soc.* **471** (2017) 3974 [[1707.04978](#)].

- [18] C.M. Trott, C.H. Jordan, S.G. Murray, B. Pindor, D.A. Mitchell, R.B. Wayth et al., *Assessment of Ionospheric Activity Tolerances for Epoch of Reionization Science with the Murchison Widefield Array*, *Astrophys. J.* **867** (2018) 15.
- [19] S.K. Pal, A. Datta and A. Mazumder, *Ionospheric effect on the synthetic epoch of reionization observations with the ska1-low*, *Journal of Cosmology and Astroparticle Physics* **2025** (2025) 058.
- [20] N.S. Kern, A.R. Parsons, J.S. Dillon, A.E. Lanman, N. Fagnoni and E. de Lera Acedo, *Mitigating Internal Instrument Coupling for 21 cm Cosmology. I. Temporal and Spectral Modeling in Simulations*, *Astrophys. J.* **884** (2019) 105.
- [21] S. Majumdar, J.R. Pritchard, R. Mondal, C.A. Watkinson, S. Bharadwaj and G. Mellema, *Quantifying the non-Gaussianity in the EoR 21-cm signal through bispectrum*, *Mon. Not. Roy. Astron. Soc.* **476** (2018) 4007 [[1708.08458](#)].
- [22] M. Kamran, R. Ghara, S. Majumdar, G. Mellema, S. Bharadwaj, J.R. Pritchard et al., *Redshifted 21-cm bispectrum: impact of the source models on the signal and the IGM physics from the Cosmic Dawn*, *JCAP* **2022** (2022) 001 [[2207.09128](#)].
- [23] A. Cooray, C. Li and A. Melchiorri, *Trispectrum of 21-cm background anisotropies as a probe of primordial non-Gaussianity*, *Phys. Rev.* **77** (2008) 103506 [[0801.3463](#)].
- [24] L. Gleser, A. Nusser, B. Ciardi and V. Desjacques, *The morphology of cosmological reionization by means of Minkowski functionals*, *Mon. Not. Roy. Astron. Soc.* **370** (2006) 1329 [[astro-ph/0602616](#)].
- [25] K.-G. Lee, R. Cen, I. Gott, J. Richard and H. Trac, *The Topology of Cosmological Reionization*, *Astrophys. J.* **675** (2008) 8 [[0708.2431](#)].
- [26] M.M. Friedrich, G. Mellema, M.A. Alvarez, P.R. Shapiro and I.T. Iliev, *Topology and sizes of H II regions during cosmic reionization*, *Mon. Not. Roy. Astron. Soc.* **413** (2011) 1353 [[1006.2016](#)].
- [27] S.E. Hong, K. Ahn, C. Park, J. Kim, I.T. Iliev and G. Mellema, *2D Genus Topology of 21-cm Differential Brightness Temperature During Cosmic Reionization*, *Journal of Korean Astronomical Society* **47** (2014) 49 [[1008.3914](#)].
- [28] S. Yoshiura, H. Shimabukuro, K. Takahashi and T. Matsubara, *Studying topological structure of 21-cm line fluctuations with 3D Minkowski functionals before reionization*, *Mon. Not. Roy. Astron. Soc.* **465** (2017) 394 [[1602.02351](#)].
- [29] S. Bag, R. Mondal, P. Sarkar, S. Bharadwaj and V. Sahni, *The shape and size distribution of H II regions near the percolation transition*, *Mon. Not. Roy. Astron. Soc.* **477** (2018) 1984 [[1801.01116](#)].
- [30] S. Bag, R. Mondal, P. Sarkar, S. Bharadwaj, T.R. Choudhury and V. Sahni, *Studying the morphology of H I isodensity surfaces during reionization using Shapefinders and percolation analysis*, *Mon. Not. Roy. Astron. Soc.* **485** (2019) 2235 [[1809.05520](#)].
- [31] B. Spina, C. Porciani and C. Schimd, *The H I-halo mass relation at redshift  $z \sim 1$  from the Minkowski functionals of 21-cm intensity maps*, *Mon. Not. Roy. Astron. Soc.* **505** (2021) 3492 [[2101.09288](#)].

- [32] A. Pathak, S. Bag, S. Dasgupta, S. Majumdar, R. Mondal, M. Kamran et al., *Distinguishing reionization models using the largest cluster statistics of the 21-cm maps*, *JCAP* **2022** (2022) 027 [[2202.03701](#)].
- [33] S. Dasgupta, S.K. Pal, S. Bag, S. Dutta, S. Majumdar, A. Datta et al., *Interpreting the HI 21-cm cosmology maps through Largest Cluster Statistics. Part I. Impact of the synthetic SKA1-Low observations*, *JCAP* **2023** (2023) 014 [[2302.02727](#)].
- [34] I.T. Iliev, G. Mellema, U.-L. Pen, H. Merz, P.R. Shapiro and M.A. Alvarez, *Simulating cosmic reionization at large scales - i. the geometry of reionization: Simulating reionization at large scales*, *Monthly Notices of the Royal Astronomical Society* **369** (2006) 1625–1638.
- [35] I.T. Iliev, G. Mellema, K. Ahn, P.R. Shapiro, Y. Mao and U.-L. Pen, *Simulating cosmic reionization: how large a volume is large enough?*, *Mon. Not. Roy. Astron. Soc.* **439** (2014) 725 [[1310.7463](#)].
- [36] S.R. Furlanetto and S.P. Oh, *Reionization through the lens of percolation theory*, *Mon. Not. Roy. Astron. Soc.* **457** (2016) 1813 [[1511.01521](#)].
- [37] K. Kakiichi, S. Majumdar, G. Mellema, B. Ciardi, K.L. Dixon, I.T. Iliev et al., *Recovering the H II region size statistics from 21-cm tomography*, *Mon. Not. Roy. Astron. Soc.* **471** (2017) 1936 [[1702.02520](#)].
- [38] W. Elbers and R. van de Weygaert, *Persistent topology of the reionization bubble network - I. Formalism and phenomenology*, *Mon. Not. Roy. Astron. Soc.* **486** (2019) 1523 [[1812.00462](#)].
- [39] S.K. Giri and G. Mellema, *Measuring the topology of reionization with Betti numbers*, *Mon. Not. Roy. Astron. Soc.* **505** (2021) 1863 [[2012.12908](#)].
- [40] A. Kapahtia, P. Chingangbam, R. Ghara, S. Appleby and T.R. Choudhury, *Prospects of constraining reionization model parameters using Minkowski tensors and Betti numbers*, *JCAP* **2021** (2021) 026 [[2101.03962](#)].
- [41] E. Komatsu, J. Dunkley, M.R. Nolta, C.L. Bennett, B. Gold, G. Hinshaw et al., *Five-Year Wilkinson Microwave Anisotropy Probe Observations: Cosmological Interpretation*, *Astrophys. J. Suppl.* **180** (2009) 330 [[0803.0547](#)].
- [42] S. Majumdar, G. Mellema, K.K. Datta, H. Jensen, T.R. Choudhury, S. Bharadwaj et al., *On the use of seminumerical simulations in predicting the 21-cm signal from the epoch of reionization*, *Mon. Not. Roy. Astron. Soc.* **443** (2014) 2843 [[1403.0941](#)].
- [43] S. Majumdar, H. Jensen, G. Mellema, E. Chapman, F.B. Abdalla, K.-Y. Lee et al., *Effects of the sources of reionization on 21-cm redshift-space distortions*, *Mon. Not. Roy. Astron. Soc.* **456** (2016) 2080 [[1509.07518](#)].
- [44] R. Mondal, S. Bharadwaj and S. Majumdar, *Statistics of the epoch of reionization (EoR) 21-cm signal - II. The evolution of the power-spectrum error-covariance*, *Mon. Not. Roy. Astron. Soc.* **464** (2017) 2992 [[1606.03874](#)].
- [45] I.P. Carucci, M.O. Irfan and J. Bobin, *Recovery of 21-cm intensity maps with sparse component separation*, *Mon. Not. Roy. Astron. Soc.* **499** (2020) 304 [[2006.05996](#)].
- [46] S. Cunnington, M.O. Irfan, I.P. Carucci, A. Pourtsidou and J. Bobin, *21-cm foregrounds and polarization leakage: cleaning and mitigation strategies*, *Mon. Not. Roy. Astron. Soc.* **504** (2021) 208 [[2010.02907](#)].

- [47] A. Bonaldi, M. Bonato, V. Galluzzi, I. Harrison, M. Massardi, S. Kay et al., *The Tiered Radio Extragalactic Continuum Simulation (T-RECS)*, *Mon. Not. Roy. Astron. Soc.* **482** (2019) 2 [[1805.05222](#)].
- [48] J.P. McMullin, B. Waters, D. Schiebel, W. Young and K. Golap, *CASA Architecture and Applications*, in *Astronomical Data Analysis Software and Systems XVI*, R.A. Shaw, F. Hill and D.J. Bell, eds., vol. 376 of *Astronomical Society of the Pacific Conference Series*, p. 127, Oct., 2007.
- [49] F. Dulwich, B.J. Mort, S. Salvini, K. Zarb Adami and M.E. Jones, *OSKAR: Simulating Digital Beamforming for the SKA Aperture Array*, in *Wide Field Astronomy & Technology for the Square Kilometre Array*, p. 31, Jan., 2009, [DOI](#).
- [50] G. Mellema, L. Koopmans, H. Shukla, K.K. Datta, A. Mesinger and S. Majumdar, *HITomographic imaging of the Cosmic Dawn and Epoch of Reionization with SKA*, in *Advancing Astrophysics with the Square Kilometre Array (AASKA14)*, p. 10, Apr., 2015, [DOI](#) [[1501.04203](#)].
- [51] S. Sridhar, W. Williams and S. Breen, *Ska low and mid subarray templates*, June, 2024.
- [52] G.B. Taylor, C.L. Carilli and R.A. Perley, *Synthesis Imaging in Radio Astronomy II*, vol. 180 (1999).
- [53] R. Braun, A. Bonaldi, T. Bourke, E. Keane and J. Wagg, *Anticipated Performance of the Square Kilometre Array – Phase 1 (SKA1)*, *arXiv e-prints* (2019) [arXiv:1912.12699](#) [[1912.12699](#)].
- [54] A. Klypin and S.F. Shandarin, *Percolation Technique for Galaxy Clustering*, *Astrophys. J.* **413** (1993) 48.
- [55] C. Yess and S.F. Shandarin, *Universality of the Network and Bubble Topology in Cosmological Gravitational Simulations*, *Astrophys. J.* **465** (1996) 2 [[astro-ph/9509052](#)].
- [56] S.F. Shandarin and C. Yess, *Detection of Network Structure in the Las Campanas Redshift Survey*, *Astrophys. J.* **505** (1998) 12 [[astro-ph/9705155](#)].
- [57] Y.B. Zel’dovich, *Origin of large-scale cell structure in the universe*, *Sov. Astron. Lett.* (Engl. Transl.); (United States) **8** (1982) .
- [58] S.F. Shandarin, *Percolation Theory and the Cell / Lattice Structure of the Universe*, *Soviet Astronomy Letters* **9** (1983) 104.
- [59] K.K. Datta, G. Mellema, Y. Mao, I.T. Iliev, P.R. Shapiro and K. Ahn, *Light-cone effect on the reionization 21-cm power spectrum*, *Mon. Not. Roy. Astron. Soc.* **424** (2012) 1877 [[1109.1284](#)].
- [60] J.V. Sheth, V. Sahni, S.F. Shandarin and B. Sathyaprakash, *Measuring the geometry and topology of large scale structure using SURFGEN: Methodology and preliminary results*, *Mon. Not. Roy. Astron. Soc.* **343** (2003) 22 [[astro-ph/0210136](#)].
- [61] J.V. Sheth, *Issues in gravitational clustering and cosmology*, Ph.D. thesis, 2, 2006. [astro-ph/0602433](#).
- [62] V. Sahni, B. Sathyaprakash and S.F. Shandarin, *Shapefinders: A New shape diagnostic for large scale structure*, *Astrophys. J. Lett.* **495** (1998) L5 [[astro-ph/9801053](#)].
- [63] G.W. Zack, W.E. Rogers and S.A. Latt, *Automatic measurement of sister chromatid exchange*

- frequency., *Journal of Histochemistry & Cytochemistry* **25** (1977) 741  
[<https://doi.org/10.1177/25.7.70454>].
- [64] M. Sezgin and B. Sankur, *Survey over image thresholding techniques and quantitative performance evaluation*, *Journal of Electronic Imaging* **13** (2004) 146.
- [65] J.-C. Yen, F.-J. Chang and S. Chang, *A new criterion for automatic multilevel thresholding*, *IEEE Transactions on Image Processing* **4** (1995) 370.
- [66] C.A. Watkinson and J.R. Pritchard, *The impact of spin-temperature fluctuations on the 21-cm moments*, *Monthly Notices of the Royal Astronomical Society* **454** (2015) 1416–1431.
- [67] S.K. Giri, G. Mellema and R. Ghara, *Optimal identification of Hii regions during reionization in 21-cm observations*, *Monthly Notices of the Royal Astronomical Society* **479** (2018) 5596  
[<https://academic.oup.com/mnras/article-pdf/479/4/5596/25218351/sty1786.pdf>].